Dalton Transactions

ROYAL SOCIETY OF CHEMISTRY

PAPER

View Article Online
View Journal | View Issue

Cite this: *Dalton Trans.*, 2026, **55**, 2574

Investigation into the viability of *N*,*N*-disubstituted-*N*′-acylthiourea copper(II) precursors for thermal deposition without the use of solvents and the affect precursor geometry has on the deposited composites

William Daly, [a,b] David J. Otway, *[a] Ian M. Povey [b] and Martyn E. Pemble[a,b]

Molecular engineering of nine closely related copper(II) *N*,*N*-disubstituted-*N*′-acylthiourea complexes (single source precursors containing pre-organised Cu–S bonding motifs) has enabled systematic optimisation of their volatilisation behaviour and thermal stability. The influence of ligand substituents, steric branching, and solid-state geometry on precursor performance was examined. All complexes are monomeric and exhibit high thermal stability, with tuneable volatility arising from structural modifications to the acylthiourea backbone. Based on thermal and vapour pressure analysis, the most promising candidates were selected for proof-of-concept solvent free Chemical Vapour Deposition (CVD), representing the first use of this ligand class in a purely thermal deposition process; previous reports employed only aerosol-assisted CVD. Under these conditions the precursors yielded a copper rich digenite ($Cu_{1.8}S$) nanocrystalline material; with a minor covellite (CuS) contribution observed, likely arising from an incompletely converted surface layer. Vapour pressure measurements demonstrate that, through appropriate ligand design, an equilibrium vapour pressure of ≈0.1 Torr can be achieved without compromising precursor stability. These results highlight *N*,*N*-disubstituted-*N*′-acylthiourea complexes as a versatile and tuneable platform for single-source precursor development.

Received 17th December 2024,
Accepted 10th January 2026

DOI: 10.1039/d4dt03482a

rsc.li/dalton

Introduction

Copper sulfide thin films and nanoparticles have been studied for a variety of uses such as solar cells,[1–8] lithium-ion batteries[9] semiconductors[10–13] and more recently biomedicine.[14,15] Copper sulfide can be synthesised in a variety of different phases, for instance: chalcocite (Cu_2S), covellite (CuS), digenite (Cu_9S_5 or $Cu_{1.8}S$), geerite ($Cu_{1.6}S$), anilite ($Cu_{1.75}S$) and villamaninite (CuS_2).[16–18] Various methods have been used to synthesise these copper sulfides and to control the stoichiometric ratio between the copper and sulfur, a tuneable ratio results in a tuneable band gap for use in optoelectronic devices.[19] Solvothermal techniques such as the use of microemulsions and vapour phase deposition methods such as Chemical Vapour Deposition (CVD) or Atomic Layer Deposition (ALD) are some of the more explored methods for copper sulfide synthesis.[14,20,21] Although the techniques may differ a common trend is the use of single source precursors (SSPs) which are attractive for being air stable, easy to handle and mostly nontoxic; they incorporate all the constituent elements,[22,23] the metal (copper) and non-metal (sulfur), in a controllable ratio to match the desired product, all in a single reagent that often has clean, low temperature decomposition routes that yield good quality nano crystallites without impurities.[23] Conventional routes to copper sulfide often require hazardous gaseous co-reagents such as hydrogen sulfide (H_2S), ammonia (NH_3) or the use of thiols (R-SH). H_2S is extremely toxic at just 10 ppm and requires specialised gas delivery and removal systems. In contrast, *N*,*N*-disubstituted-*N*′-acylthiourea complexes are non-volatile (at RT), air and light stable solids that can be weighed, stored and transferred under standard laboratory conditions. The SSP approach used here eliminates the need for any external sulfur agent, simplifying handling and improving operational safety. Preliminary cytotoxicity screening of the metal complexes (**A–K**) and corresponding organic ligands (SI Fig. S1) shows low to moderate toxicity against HEK293 cells; consistent with their benign handling properties; with compound (**F**) flagged as an outlier. There are several ligands commonly used as SSPs for metal sulfides such as thiolates,[24] dithiocarbamates,[25,26] xanthates,[27] dialkychalco-

[a]*School of Chemistry, University College Cork, Cork, Ireland.*
E-mail: dave.otway@ucc.ie
[b]*Tyndall National Institute, Cork, Ireland*

genophosphates,[28] thiobiurets,[18,29] dithiobiurets[30,31] and *N*,*N*-disubstituted-*N*′-acylthiourea.[32] Many of these SSPs have been used in aerosol-assisted CVD (AACVD)[21,33] where the precursor is dissolved in an appropriate solvent and vaporised while in a nebulizer for transport to the substrate. AACVD eliminates the need for SSPs to be quite volatile and focuses more on their solubility. The thermal properties and sensitivity of these precursor systems vary widely. For example, thiolates often exhibit low decomposition onset temperatures (≈130 °C) and significant air/light sensitivity; while xanthates undergo Chugaev elimination at similarly low temperatures. Dithiocarbamates and diphosphine disulfide complexes typically show greater thermal robustness resulting in higher deposition temperatures (350–500 °C). In this context, the Cu(II) *N*,*N*-disubstituted-*N*′-acylthiourea complexes (**A–K**) reported here offer a distinct balance of air stability, clean decomposition pathways and competitive thermal windows relative to established SSP classes (SI Table S1[21,32,34–47]). Herein we investigate how structural modifications within this ligand family influences precursor volatility and examine potential correlations between solid state geometry, physical properties and the composition of the resulting nanocrystalline copper sulfide films.

Tuning knobs for precursors

The properties of a precursor play a key role in the vapour deposition technique. These essential properties include sufficient volatility and thermal stability.[48,49] Although such characteristics might be deemed the most important, there are many other attributes that should also be considered (see Fig. 1).

These requirements are characteristic of a successful precursor. Volatility is needed for efficient transport between the bubbler and the reaction chamber. Deposition processes can occur at a range of temperatures. Thermal stability is important to ensure the precursor does not decompose in the temperature range of the growth cycle or when entering the chamber. If the precursor is not thermally stable the temperature difference from when it leaves the bubbler to when it enters the chamber can cause it to decompose. The volatility and thermal stability combined should provide a suitable temperature window in which the precursors vapour pressure can be extracted over long periods of time without decomposing or degrading. Once chemisorbed onto the substrate surface the growth cycle continues but what happens to the by-products. By-products from a growth cycle should ideally be volatile, unreactive, and carried away by the inert carrier gas N_2, Ar. Reabsorption of the by-products can result is a slow film growth and the incorporation of impurities into the film. Precursors that contained halogens can form HCl, or HF, substances that can corrode the inside of the reactor. A good precursor should neither etch the growing film nor be incorporated into the film ensuring a pure film is grown. Every application has its own requirements and with that comes specific purity requirements of the precursor. Therefore, a precursor should be of suitable purity; containing inexpensive ligands and is relatively easy to synthesize and scale up. The last two requirements are rarely ever met, and this is due to the very nature of the materials themselves; non-explosive and non-toxic precursors are difficult to source. This is normally compensated by their inherent high reactivity and volatility. Precursors of high reactivity are very attractive because film growth proceeds at lower temperatures and at faster rates.

Precursor design

Precursors can be tailored for selective film deposition with slight modifications to the ligands on the precursors can changing the properties leading to a potentially suitable precursor for thermal deposition techniques. One of the most important guidelines is to keep the molecular weight low when considering volatility. Volatility can be linked to intermolecular forces such as van der Waals, hydrogen bonding, and pi interactions. Monomers can have a higher volatility than their dimer and

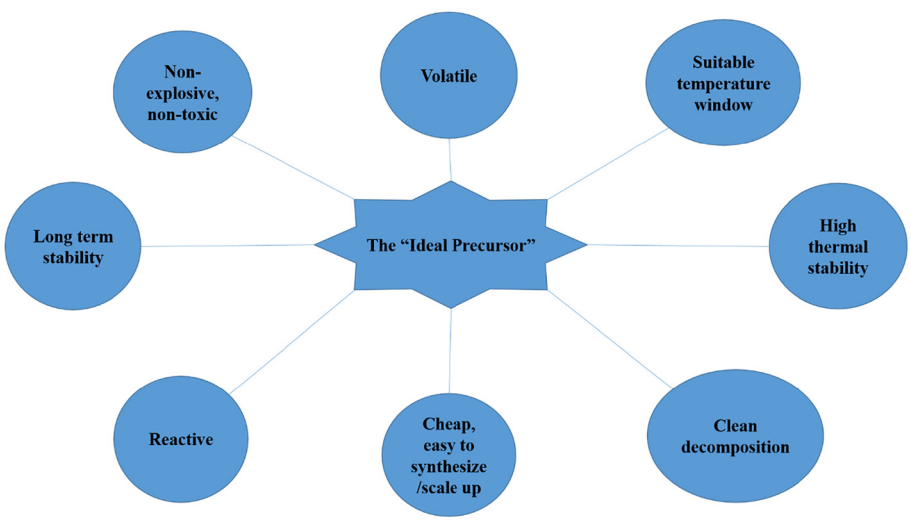

Fig. 1 Requirements of a successful precursor.

polymer counterparts. One strategy for enhancing volatility is by introducing bulky ligands such as long, low branched or unbranched alkyl chains.[49] Through the introduction of these, the intermolecular forces that lead to dimers, oligomers and polymers are reduced along with the melting point of the precursor. To form a monomer a molecules coordination sphere needs to be saturated and this can be challenging for monodentate ligands. However, using low branched chains and bulky groups results in a successful blocking of the metals coordination sites as seen in the alkoxide and alkylamide below (see Fig. 2). The alkoxide shows only one substituent bound to the hetero atom, whereas the dialkylamide has two substituents therefore providing a greater steric demand. Due to this demand more coordination sites on the metal become sterically hindered (red triangles represent blocked sites).

It is difficult to form monomers using monodentate ligands as; depending on a metals ionic radius and oxidation state, steric bulk from the ligands might not hinder all possible coordination sites. To satisfy this neutral donor ligands maybe used. The donor ligand satisfies the coordination sphere, does not affect the metals oxidation state and in many cases stabilises a precursors reactivity if the donor remains coordinated. Common donor ligands include tetramethylenediamine (TMEDA), or diglyme (see Fig. 3).

A second way to reduce the melting point of the precursor is by altering the entropy change of crystallisation.[50,51] Reducing the precursor symmetry and adding an element of asymmetry *via* short branched chains as discussed above, can force them to adopt a more specific lattice conformation, frustrating the crystallization process and resulting in a lowered melting point.[50]

The use of bidentate chelating ligands can also saturate a metals coordination sphere, aiding in the synthesis of monomeric units. Some examples of bidentate ligands, β-thioketonates, monothiocarbonates and *N*,*N*-disubstituted-*N*′ acylthiourea below (see Fig. 4).

The use of bidentate ligands leads to an increased thermal stability, but possibly also a lack of volatility. "However, the development of a thermally stable precursor often relies largely on guess and check".[52] In designing precursors for vapour deposition, several structural "tuning knobs" can be adjusted to balance volatility, stability, and decomposition behaviour. Among these, three factors are particularly critical; (i) melting point, which governs ease of handling and dosing; (ii) entropy of crystallisation, which influences solid state packing and phase transitions; and, (iii) steric branching, which modulates intermolecular interactions and volatility. In the following results section, each of these aspects is examined in detail to illustrate how subtle structural modifications within the acylthiourea backbone translate into measurable differences in precursor performance.

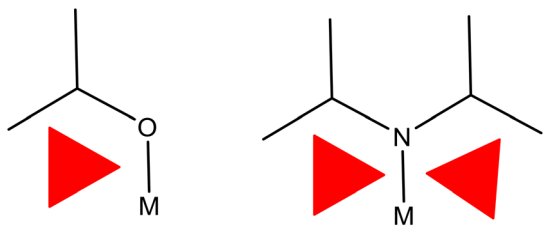

Fig. 2 Schematic of alkoxide and alkylamine moieties. The red triangles represent regions in space potentially blocked off due to the single bond rotations from the ligands.

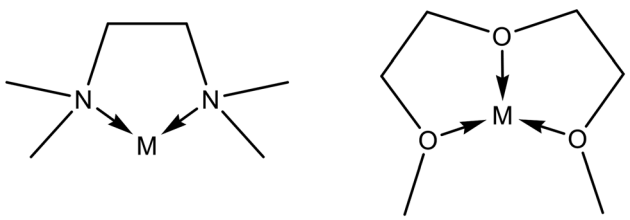

Fig. 3 Schematic of dative ligands TMEDA (left), diglyme (right) encapsulating a metal centre.

Results and discussion

Melting point

A low melting point is usually ideal for precursor compounds; the best precursors melt between room temperature and the processing temperature.[49,53] Thermal deposition processes such as ALD, AACVD, require repeatable precursor dosing for

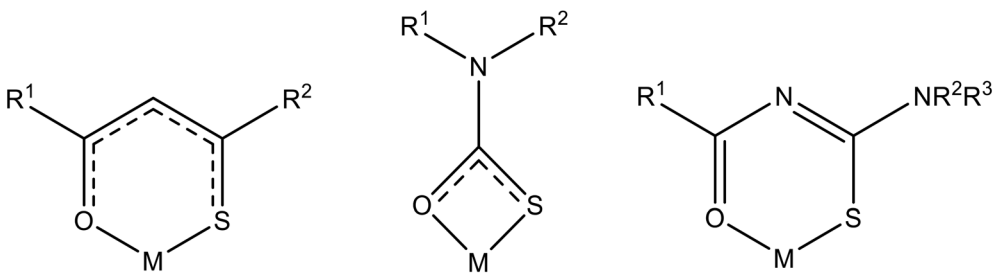

Fig. 4 Lewis structure of oxygen sulfur based bidentate ligands coordinating to a metal centre through both oxygen and sulfur hetero atoms β-thioketonates (left), monothiocarbonates (middle) and *N*,*N*-disubstituted-*N*′acylthiourea (right).

each pulse to ensure full saturation of the substrate surface is always achieved without excessively long pulse times. This window allows the precursor to be easily transported and stored as a solid but used for deposition as a liquid because liquids generate a more constant vapour pressure as they maintain a constant surface area whilst the precursor is depleting. Surface area has a direct effect on the kinetics of volatilisation, solid precursors depend on particle size, crystalline or powder (and how fine a ground powder they are).[49] Particle size may differ from batch to batch and the vapour pressure may differ unpredictably as a result. Solids can also absorb impurities on their surface during volatilisation, thus hindering their volatility.

There are several strategies for modifying melting points and most of them require subtle adjustments to the precursor structure.

Entropy of crystallization. By reducing the symmetry of a precursor, the molecules can be forced to adopt a more specific conformation in the solid state, and this upsets crystallization patterns and may result in a lowering of the melting point.[50]

Branching. Inclusion of long, low-branched, or unbranched alkyl chains allows the compound to become highly mobile in the liquid phase, making melting more entropically favourable and this can also reduce intermolecular interactions in the crystal lattice by sterically shielding the metal centre.[50]

It is worth noting that these methods of modifying a precursor can act as a double-edged sword. Long branched alkyl chains also add to the overall molecular weight, in general a compound with a larger molecular weight needs more energy to go from solid to liquid this usually results in increasing the melting point (Fig. 5).

Branching effects

Group 1. Compounds (**A** & **C**) have the same melting point of 115–118 °C, although they differ in molecular weight by 112.22 g mol^{-1}, this shows the low branched chain with diiso-butyl has the same melting point effect as the lower molecular weight *di*ethyl group. Compound (**B**) has the adverse effect with the iso-propyl group. It has the highest melting point and is also the only *trans* geometry compound from this group.

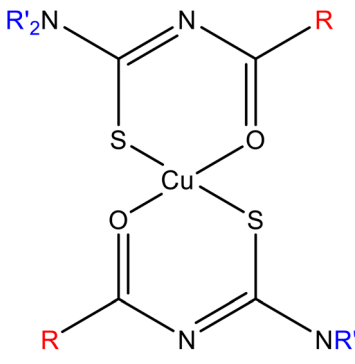

Fig. 5 Skeletal structure of a general copper(II) *N*,*N*-disubstituted-*N*′-acylthiourea precursor.

Group 2. Compound (**F**) has the lowest melting point while compound (**D**) has the highest, mapping a similar trend to group 1 with the compounds having R′$_2$ groups of diethyl and diiso-propyl respectfully. Group 2 follows the trend as the number of carbons in the chain increases the melting point increases.

Group 3. Shows somewhat of a reverse trend, compound (**G**) which is the most shielded with the highest number of carbons in the side chain has the lowest melting point, while compound (**K**) being the least sterically hindered and fewest carbons in the R′$_2$ side chain has the highest melting point.

Observations. Comparing groups 1 & 2 specifically compounds (**C** & **F**) the melting points vary by 4 °C while both compounds adopt a *cis* geometry. From this one could postulate that the melting point effect between a *tert*-butyl and a phenyl group is negligible. However, applying the same justification to compounds (**B** & **D**) the proposal breaks down, with the melting point difference between these compounds is 37 °C. This is significant enough and we hypothesis that although the compounds do have different molecular weights one key difference is their respective geometry, *trans* (**B**) and *cis* (**D**). The different geometries could link back to the entropy of crystallisation which cannot be ruled out as factor for precursor assessment. It is also apparent that in both groups the diiso-propyl substituent compounds exhibit the highest melting points showcasing that it does not perform particularly well.

Comparing the groups 2 & 3, compounds (**E** & **G**), these are very similar structurally, both having a *trans* geometry. Their melting points differ by 10 °C. This subtle difference can be attributed to the slight molecular weight increase as we move from phenyl to mesityl. The melting point effect going from phenyl to mesityl is not negligible, but it is small $\Delta T_{\text{mesityl-phenyl}} = 10$ °C.

Comparing the compounds with the same R′$_2$ groups, compounds (**C**, **F**, & **H**), a large change in melting point range is seen for compound (**H**) of over 100 °C. It has been already established that the order in which the branching of an R group affects the melting points was as follows, *tert*-butyl ≈ phenyl ≥ mesityl, but compound (**H**) shows that this only holds if the compounds are also the same geometric configuration. Unfortunately, it was not possible to quantify the impact molecular geometry had due to other factors such as molecular weight but there is possibly a connection between the potential precursor geometry and their physical properties. A comparison of all three groups together, comparing their melting points as a function of number of carbons on the R′$_2$ chain showed that **A**, **C**, **F** and **B** have the lowest melting points and hence the most potential as suitable precursors (Fig. 6).

Molecular weight

Volatility is a prerequisite for both CVD and ALD precursors. Volatility is affected by intermolecular forces, (van der Waals, π-stacking, hydrogen bonding *etc.*). These forces are influenced by molecular weight, geometry and for solid precursors, the lattice structures. Typically, vaporisation temperature increases

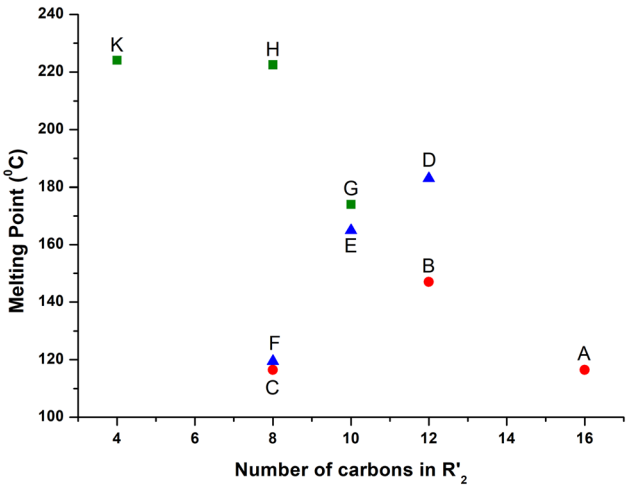

Fig. 6 Melting point as a function of number of carbons off the exocyclic amide moiety per ligand of all compounds (A–K). Group 1 Compounds A, B, C labelled with red circles, Group 2 Compounds D, E, F labelled with blue triangles, Group 3 Compounds G, H, K labelled with green squares.

with molecular mass as more energy is needed to cause a phase change from solid or liquid to vapour. Fig. 7 below maps the molecular weight of each precursor against the temperature observed at 50% mass loss.

Group 1. Follows the general trend, *i.e.* increase molecular weight results in an increased temperature, except for compound (**B**) which has the lowest decomposition temperature of all the precursors.

Group 2. Spanning the smallest molecular weight window of all three groups, a similar trend to that seen in group 1 is observed, linear increase except for compound (**E**).

It is worth noting once again that compounds (**B** & **E**) are the only *trans* geometry in their respective groups, indicating that structural geometry could play a part in precursor volatility.

Group 3. Follows a linear trend increase except for compound (**G**) which has the largest molecular weight of all the precursors. All compounds in group 3 have the same *trans* structural geometry, other intermolecular forces must be considered to explain why compound (**G**) breaks the trend.

Crystal packing and hirshfeld surface analysis (HSA)

Across the nine complexes (**A–K**), a clear relationship emerges between crystal symmetry, molecular geometry and thermal behaviour see summary table below (Table 2). Compounds crystallising in the $P2_1/c$ space group; particularly those with *trans* geometry such as compound (**B, G, H** & **K**) consistently exhibit tighter packing and stronger intermolecular interactions, which correlate with higher melting points and reduced volatility. *Cis* compounds such as compounds (**A, C** & **F**) all adopt the low symmetry $P\bar{1}$ space group, show looser packing and weaker contacts, reflected in their low

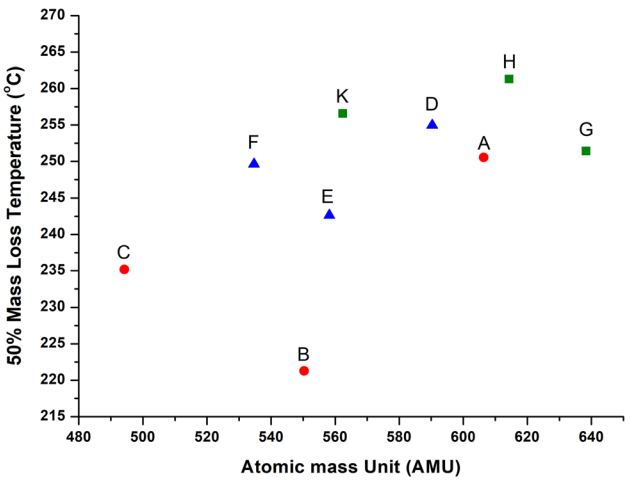

Fig. 7 Thermogravimetric analysis as a function of molecular mass for compounds (A–K).

Table 1 Summary of the nine copper(II) compounds, their grouping, geometry and alkyl substituents

	Compound	Geometry	R	R'_2	Melting point (°C)
Grp 1	(**A**)	*Cis*	*tert*-Butyl	iso-Butyl	115–118
	(**B**)	*Trans*	*tert*-Butyl	iso-Propyl	145–149
	(**C**)	*Cis*	*tert*-Butyl	Ethyl	115–118
Grp 2	(**D**)	*Cis*	Phenyl	iso-Propyl	182–184
	(**E**)	*Trans*	Phenyl	Piperidine	164–166
	(**F**)	*Cis*	Phenyl	Ethyl	119–120
Grp 3	(**G**)	*Trans*	Mesityl	Piperidine	173–175
	(**H**)	*Trans*	Mesityl	Ethyl	221–224
	(**K**)	*Trans*	Mesityl	Methyl	223–225

Table 2 Summary of crystal space groups, geometries, and packing implications for compounds (A–K)

Compound	Geometry	Space group	Symmetry class	Packing implication
A	*Cis*	$P\bar{1}$	Triclinic	Loosely packed, low symmetry
B	*Trans*	$P2_1/c$	Monoclinic	Tightly packed, directional bonding (HSA)
C	*Cis*	$P\bar{1}$	Triclinic	Weak packing, low symmetry
D	*Cis*	$P2_1/c$	Monoclinic	Efficient packing, high MP
E	*Trans*	$P2_1/n$	Monoclinic	Moderate packing, disrupted by piperidine
F	*Cis*	$P\bar{1}$	Triclinic	Weak packing, low MP
G	*Trans*	$P2_1/c$	Monoclinic	Strong packing, high MP
H	*Trans*	$P2_1/c$	Monoclinic	Strong packing, high MP
K	*Trans*	$P2_1/c$	Monoclinic	Strong packing, high MP

melting points (MP) and greater volatility. Notably, compound (**D**; *cis*; $P2_1/c$) defies the typical trend most likely due to its efficient packing and favourable substituent orientation, resulting in a melting point higher than its group counterparts compounds (**E** & **F**). These observations highlight that crystal symmetry and packing efficiently, rather than molecular weight alone, play a more critical role in governing precursor behaviour.

Thermalgravimetric analysis

Thermal gravimetric analysis (TGA) is a very useful analysis technique used in precursor design as TGA can measure volatility and observe a step-by-step decomposition through first derivatives. Fig. 8 shown below shows the TGA profiles (along with the first derivatives) of each compound (**A–K**) and a summary of the thermal data are given in Table 3; values are obtained from Differential Scanning Calorimetry plots see SI Fig. 2.

Group 1. Compound (**B**) is the only sample that decomposes in a single step over the temperature range 155–320 °C. It has a mass loss of 84.96% with a residual mass of 15.04%. The nonzero residual mass indicates that decomposition did occur. From the corresponding differential scanning calorimetry (DSC) profiles see SI Fig. 2 endothermic peaks for the phase change melting process at 143–151 °C, and the decomposition process at 220–233 °C are seen. The lack of sharpness and definition for the second peak indicates that it was undergoing a decomposition process.

Compound (**A**) shows a two-step decomposition curve, with a sharp initial drop between 190–260 °C with a mass loss of around 70%, and a second more gradual drop between 260 °C–330 °C with a 20% mass. Compound (**A**) has the highest mass loss out of all nine complexes and the smallest residue, below 10% which is good amongst the precursors tested. The first mass loss step exhibits traits of pure volatilisation, straight line drop increasing exponentially, but the non-zero residual mass indicates some decomposition occurred.

Compound (**C**) follows a very similar thermal profile to that of compound (**A**), a two-step decomposition with the first initial drop between 195–240 °C with an accompanying mass loss of 60%, its second step occurs between 240–262 °C with a 23% mass loss.

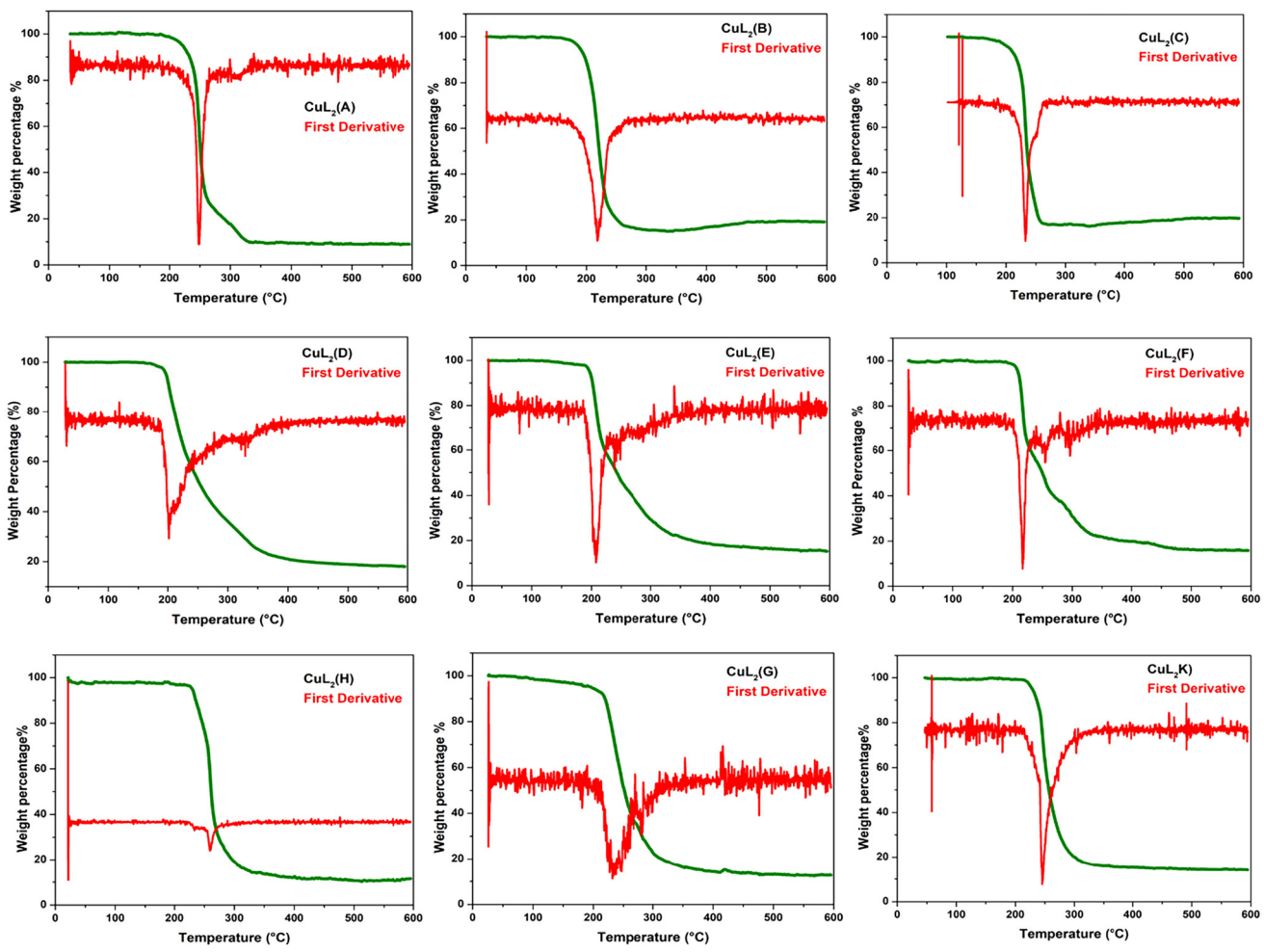

Fig. 8 Thermogravimetric analysis and 1st derivative of nine potential precursors for all compounds (**A–K**).

Table 3 Summary of thermal data for all compounds (A–K)

Compound & Groups		Onset temperature of decomposition (°C)	Decomposition range (°C)	1st derivative	Mass loss (%)	Residue (%)
Group 1	(**A**)	239	239–329	2 step	90.9	9.1
	(**B**)	203	203–264	1 step	84.96	15.04
	(**C**)	223	165–255	2 step	82.95	17.05
Group 2	(**D**)	194	195–450	2/3 step	81.13	18.44
	(**E**)	192	193–438	2/3 step	84.28	15.82
	(**F**)	211	211–470	3 step	83.73	16.08
Group 3	(**G**)	213	213–335	2 step	84.19	12.66
	(**H**)	227	227–319	2 step	89.16	10.69
	(**K**)	225	225–304	2 step	83.40	14.56

Group 2. All compounds in this group exhibit a three-step decomposition, which can be hard to identify as there is no distinctive change due to the curvature in their thermal profiles, but the derivative curves do indicate a three step, albeit step 2 and step 3 are hard to identify. This group has the largest decomposition range of over 200 °C (see Table 3), with compound (**F**) having a decomposition range spanning 290 °C, the largest amongst all nine complexes. Although the decomposition steps occur at different temperatures a trend in the mass loss at each step emerges for these compounds, with each compound losing ≈35%, ≈25%, ≈23%, for their first, second and third decomposition steps. The curved shape to the thermal profiles makes these compounds undesirable as potential precursors, but the trend in the mass loss for each step could be used to map a potential breakdown pathway for precursors with similar backbone ligands. Understanding the

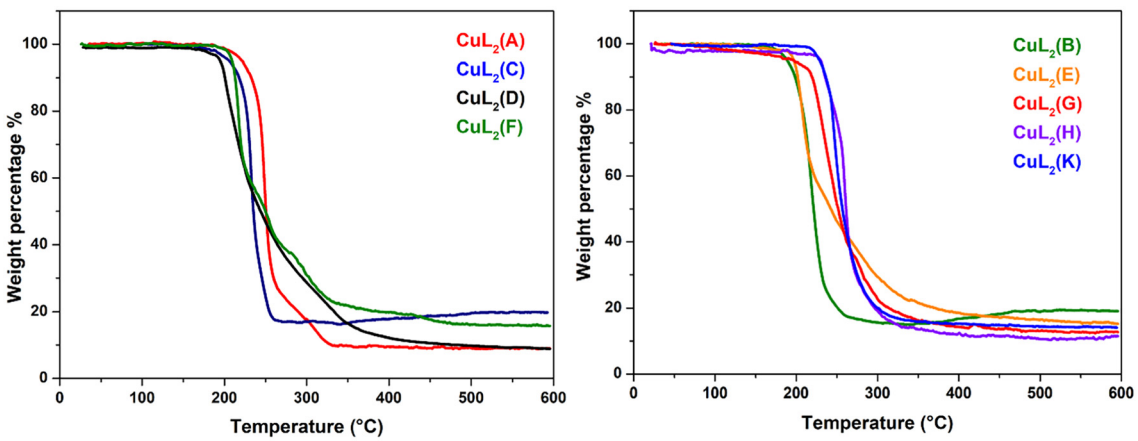

Fig. 9 TGA plots of *cis* compounds (**A**, **C**, **D**, **F**) (left), TGA plots of *trans* compounds (**B**, **E**, **G**, **H**, **K**) (right).

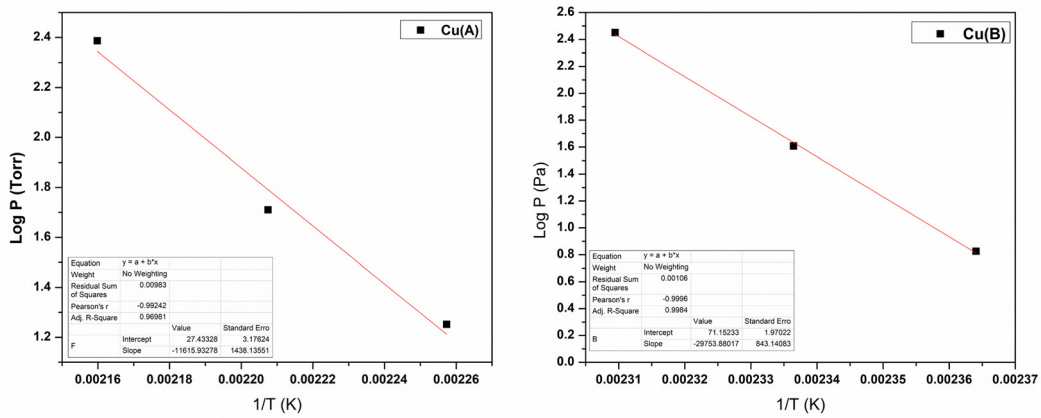

Fig. 10 Vapour pressure plots for precursor **A** (left) and **B** (right).

thermal breakdown pathway can help in the redesign of a precursors backbone and as a result could eliminate the structural characteristic that is causing an unwanted residue.

Group 3. All three compounds (**G**, **H**, **K**) have two-step decomposition thermal profiles, with compounds (**H**) and (**K**) having similar shaped mass loss curves, these being a gradual slope before declining into a steeper slope for the second decomposition step, whereas compound (**G**) has a profile like those in group 2. Group 3 has some of the lowest % residue of all complexes tested, and compounds (**H** & **K**) have the smallest temperature difference between their melting phase and decomposition phase but do have the highest melting points as discussed previously.

Precursor selection

Based on the selection criteria of what makes a suitable precursor, the requirements for CVD, and the topics discussed previously, some of the compounds tested would be considered potential candidates to take forward for growth studies. From the melting point and molecular weight data compounds (**A**, **B**, **C**, **E** & **F**) had potential. The thermogravimetric analysis data is hugely important in precursor selection and as discussed; based on their thermal profiles' compounds (**E** & **F**) are unfavourable.

A comparison of the precursor's geometry with their physical properties and crystallite decomposition is shown in Fig. 9, where all *cis* and *trans* geometry arrangements are included. Compound (**B**) was selected as the *trans* precursor to bring forward for growth studies, as it has a reasonable melting

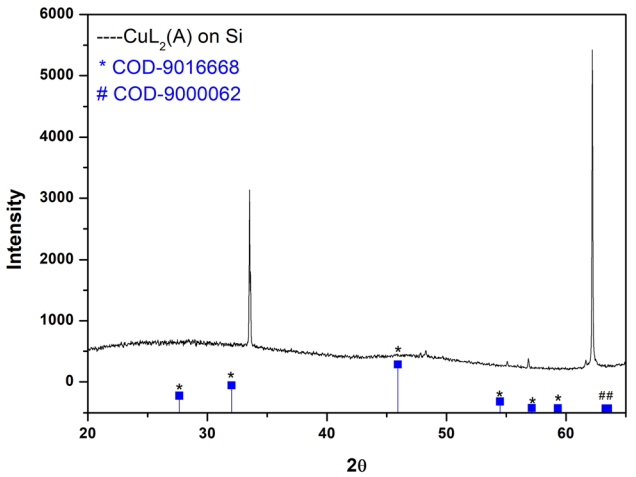

Fig. 11 XRD pattern of copper sulfide deposit formed from precursor (**A**) with COD references for both digenite and covellite.

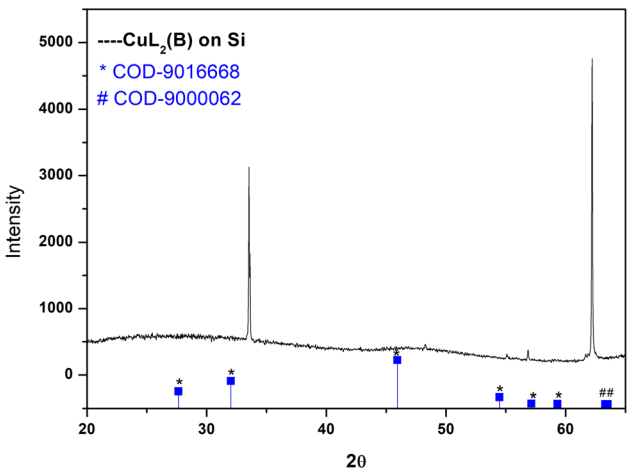

Fig. 12 XRD pattern of copper sulfide deposit formed from precursor (**B**) with COD references for both digenite and covellite.

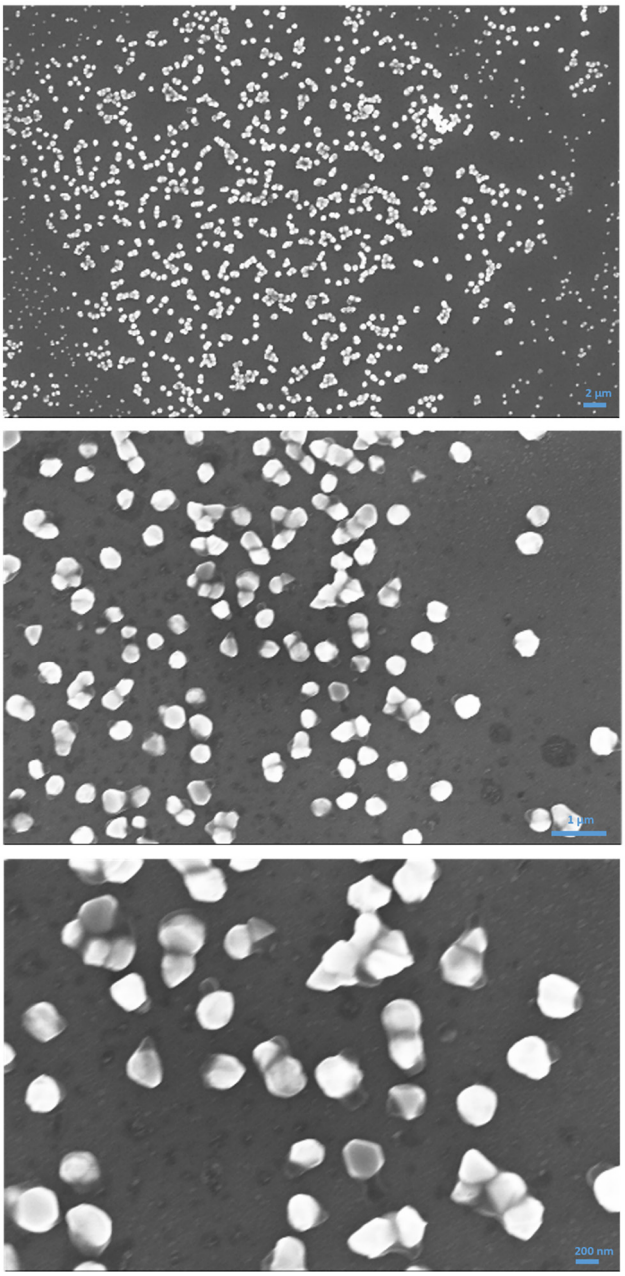

Fig. 13 SEM images of the deposit grown at 230 °C from precursor (**A**).

point, the ligand backbone has branched alky chains, (**B**) molecular weight is relatively small compared to the other potential precursors and it has one of the lowest decomposition temperatures. For the *cis* precursor it was difficult to decide between compound (**A**) or (**C**), but ultimately compound (**A**) was chosen for having a similar decomposition range to compound (**B**), their respective branched alkyl chain lengths for the R'_2 groups only differing by a $(CH_2)_n$ unit and for its ease of synthesis.

Precursor vapour pressure

A suitable vapour pressure is a sought-after characteristic for precursors when it comes to thermal deposition techniques. From the proof of principle experiments it was clear both precursors (**A** & **B**) have the capability to grow copper sulfide composites, but for a larger substrate in a reactor vessel, the choice of precursor transport must be considered. Isothermal TGA experiments were performed on both precursors (see SI Fig. S3).

Precursor (**A**) exhibited a consistent linear weight loss over a 90-minute period at a 170 °C. A similar result can be seen at 180 °C but only for around 60 minutes, then a drop in weight was observed, indicating a shift in the precursors vapour equilibrium. At 190 °C a linear weight loss was observed but only for 20 minutes before it shifted to resemble a thermal decomposition curve. Precursor (**B**) showed a linear trend at 150 °C for the full 90 minutes and for most of the time at 155 °C. At 160 °C precursor (**B**) showed a thermal decomposition curve. For both precursors the lowest temperatures of 170 °C and 150 °C respectively have the best linear regression. Once the temperature increased; the linear depletion was not maintained for the full 90 minutes as the precursors window of decomposition was being approached (see SI Table S2).

From a combination of the isothermal TGA results and use of the Knudsen equation and the Clausius–Clapeyron equation a vapour pressure plot was constructed for each precursor (see Fig. 10).

From these plots it is possible to gauge what kind of vapour pressure the precursors would have at a given temperature inside a deposition reactor. The precursor must have a vapour pressure that is practicable, especially if it is to be used with a pulsed delivery system. If the precursor loading was fully vaporised after one pulse; all of the compounds will have been used up, making the growth experiment unsustainable and impractical. Control over how much of the loading is vaporised and pulsed efficiently is instrumental in CVD.

The Ideal vapour pressure for a precursor is "at least 0.1 Torr equilibrium vapour pressure"[54] at a temperature where the precursor does not decompose thermally. From the

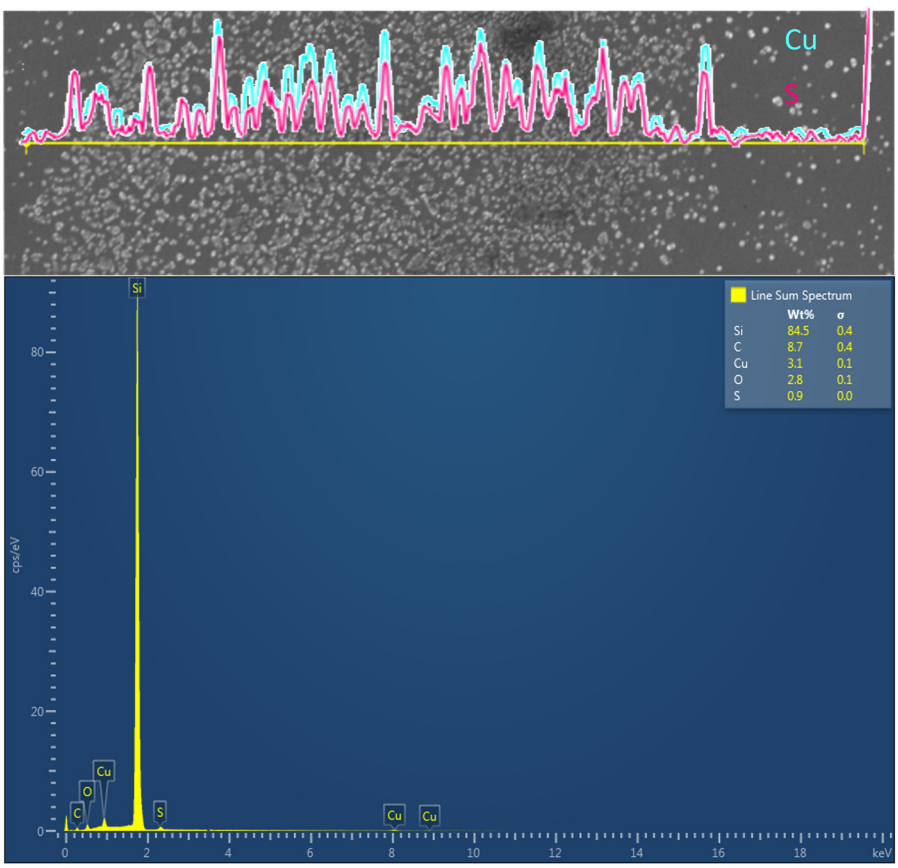

Fig. 14 Line EDX of particle region grown at 230 °C from precursor (**A**).

straight-line plots shown above in Fig. 8, it is estimated that both precursors will have a vapour pressure of 0.1 Torr at a temperature of ≈175 °C for precursor (**A**) and ≈154 °C for precursor (**B**). At these temperatures both precursors (**A** & **B**) are thermally stable and would have gone through a melting phase (see Table 1), ensuring that as liquids they will have a steady vapour pressure and will not fluctuate.

To place these findings into context, the thermal behaviour of our selected precursors can be benchmarked against established single source classes, precursors (**A** & **B**) volatilise cleanly, combining competitive volatility with enhanced air stability. If one was to compare them with those listed in SI Table S1, *N*,*N*-disubstituted-*N*′acylthiourera complexes bridge the gap between highly volatile but unstable thiolates and more the more robust but less volatile dithiocarbamates.

Materials deposition

Proof of principle

The selected precursor compounds (**A** & **B**) were placed inside alumina boat crucibles, and a pre-cleaned silicon wafer was placed on top of the crucibles, polished side facing down. The crucibles were placed inside a quartz tube that was then inserted into a tube furnace and heated in air for three hours (Schematic overview of the thermal CVD setup used in this work is provided in the SI Fig. S4). Precursor (**A**) was heated to 230 °C while precursor (**B**) was heated to 190 °C. The furnace was left cool to room temperature before the crucibles were removed.

Thermal CVD of precursors (**A** & **B**) resulted in the formation of crystalline copper sulfide films produce crystalline copper sulfide films directly on the silicon substrates. XRD patterns for both deposits are shown in Fig. 11 and 12, with reference patterns for both digenite (COD 9016668) and covellite (COD 9000062) included with scaled relative intensities. Both samples exhibit characteristic reflections of copper-deficient digenite type $Cu_{1.5-1.8}S$ phases consistent with the expected thermolysis of *N*,*N*-disubstituted-*N*′-acylthiourea complex (see SI Table S1). The XRD peaks are slightly shifted from the reference due to the copper deficiency within the film, the deficiency increases vacancy concentrations on copper sites contracting the average lattice shifting the 2θ to higher values. The higher 2θ peaks observed in both XRD patterns are from sulfur rich covellite. Digenite is thermodynamically favoured; the surface of the digenite can react with residual sulfur or sulfur containing species (possibly volatiles from the precursor thermal breakdown pathway) producing a more sulfur rich environment and thus resulting in a thin capping layer of covellite CuS which is a more kinetically favoured form. The capping covellite layer acts as a self-limiting surface reaction with factors such as precursor flux and dose percentage also having an impact.

Scherrer analysis was applied to all observed reflections of both deposits to estimate crystallite size (see SI Tables S3 an S4). Deposits from precursor (**A**) exhibit larger crystallites (average 104 nm) whereas precursor (**B**) produces smaller crystallites (average 5 nm) across all analysed reflections. The contrast in crystallite size reflects differences in the nucleation and growth behaviour of the two precursors under thermal activation.

Measured *d*-spacings extracted from the main reflections of each deposit (see SI Tables S5 and S6) show a close agreement with COD-9016668. For precursor (**A**) the experimental *d*-spacing match a digenite variant with shifts consistent with the copper deficient sublattice. Precursor (**B**) like (**A**) matches a copper deficient digenite variant.

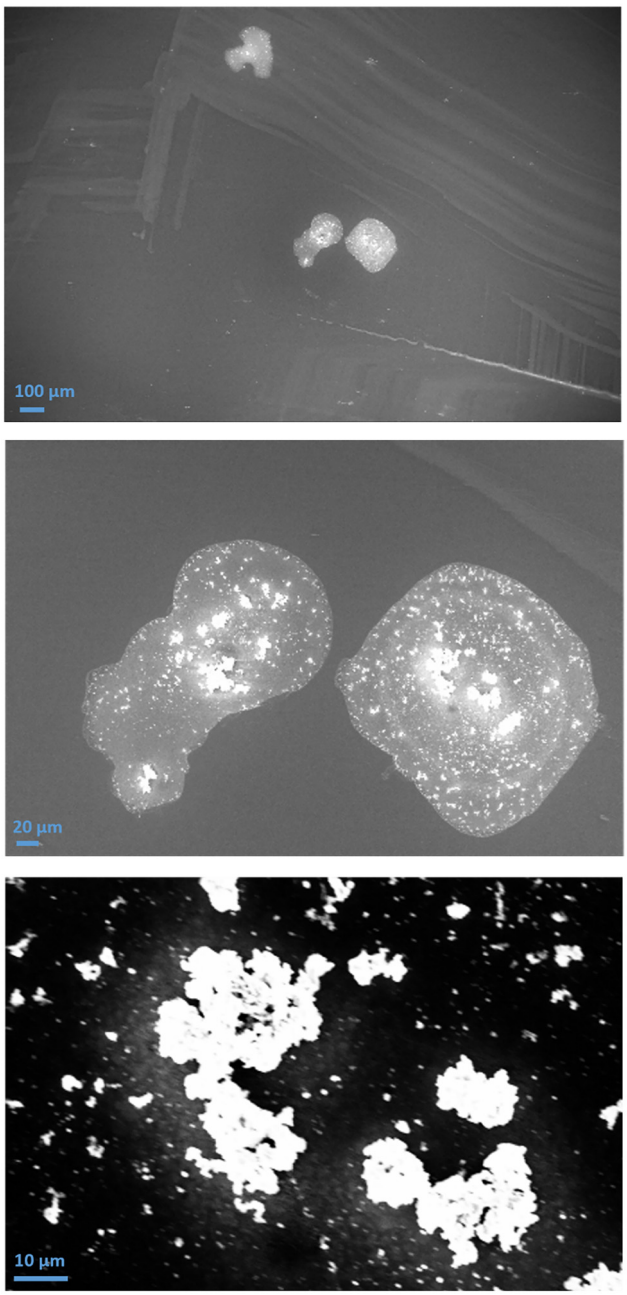

Fig. 15 SEM images of deposit grown at 190 °C from precursor (**B**).

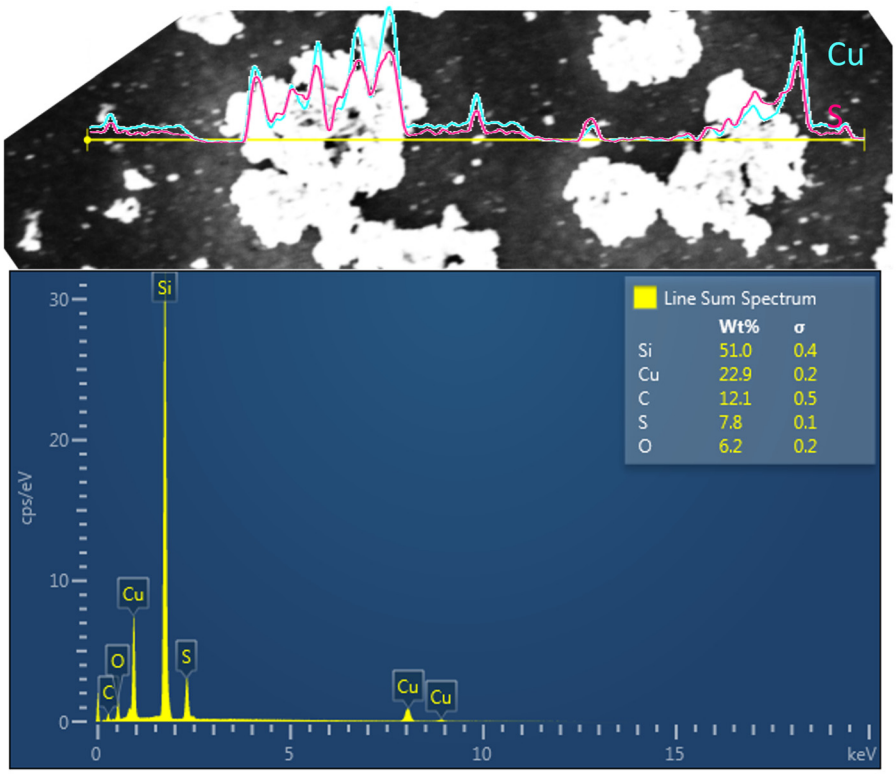

Fig. 16 Line EDX of particle region grown at 190 °C from precursor (**B**).

Scanning Electron Microscopy (SEM) analysis of precursor (**A**) despite having larger crystallites display a more uniform, continuous aggregation of nano spherical particles across the substrate (see SEM Fig. 13); the particles appeared to be arranged on regions where the wafer was directly over the precursor. In the Energy Dispersive X-ray analysis (EDX) focused on different areas of the substrate, both copper and sulfur were observed in the synthesised nanocomposites across the line scan (see Fig. 14). The measured atomic percentage for the element quantities of Si, O, C, Cu, S were 75.5%, 4.39%, 18.18%, 1.22% and 0.70% respectively, giving a Cu: S ratio of 1.74 : 1. The ratio provides further evidence for the copper deficient digenite variant.

Conversely, deposits from precursor (**B**) present an island type morphology (see Fig. 15), where smaller crystallites coalesce into discrete clusters rather than forming continuous coverage. This growth is consistent with rapid nucleation producing many small crystallites that subsequently aggregate locally, giving rise to discontinuous surface coverage despite the finer crystallite size. EDX analysis once again confirmed the presence of copper and sulfur *via* line scan (see Fig. 16), with observed atomic percentages of Si, O, C, Cu, S being 48.66%, 10.09%, 25.54%, 9.40%, and 6.29% resulting in a copper to sulfur ratio of 1.49 : 1.

SEM, EDX and Scherrer analysis therefore provide complementary insights; precursor (**A**) yields large crystalline domains but a smoother, more uniform film, while precursor **B** yields smaller crystalline domains that assemble into clustered surface islands.

The contrasting behaviours of precursors (**A** & **B**) can be rationalised by considering their solid-state geometries, ligand environments and thermal decomposition pathways. The more rigid coordination environment of precursor (**A**) favours a clean thermolysis that generates fewer nucleation centres, resulting in larger crystallite domains that combine into uniform films. In contrast, precursor (**B**), which decomposes potentially *via* a more stepwise manner and at slightly higher temperatures, liberates copper–sulfur fragments at a faster rate, producing a high density of nucleation sites. This leads to smaller crystallites but promotes island growth as clusters rapidly form and combine locally. The observed *d*-spacing shifts support differences in copper occupancy within the digenite lattice, while the TGA residue trends reflect the relative cleanness of decomposition. Taken together these results demonstrate how subtle variations in precursor structure and decomposition energetics can modulate nucleation kinetics, crystallite size, and eventual film morphology, highlighting the importance of precursor design in controlling copper sulfide growth under solvent-free thermal CVD conditions.

The contrasting deposition behaviours of precursors (**A**) and (**B**) suggest different application niches. Precursor (**A**), which yields larger crystallites and more uniform film coverage, is well suited to optoelectronic and photovoltaic applications where continuous films with fewer grain boundaries

are desirable to minimise charge carrier scattering and recombination. The reduced grain boundary density in these larger crystallites facilitates efficient charge transport, improving conductivity and device performance. In contrast, precursor (**B**) produces smaller crystallites and discontinuous, clustered growth, which may be advantageous for catalytic or sensing applications where a high density of grain boundaries and surface sites enhances reactivity. The increased grain boundary population in these deposits provides more active sites for adsorption and reaction, making them attractive for electrochemical devices or heterogeneous catalysis. Thus, while both precursors form copper digenite phases, their distinct crystallite sizes and growth morphologies point to complementary application spaces: (**A**) for uniform thin film technologies and (**B**) for nanostructured, surface active systems.

Conclusion

Nine *N*,*N*-disubstituted-*N*′-acylthiourea copper(II) precursors (**A–K**) were synthesised and systematically evaluated for their physical properties. Both steric branching and molecular geometry were found to exert a strong influence on volatility and melting point. While branched alkyl chains have been studied previously, our work highlights that geometric configuration (*cis vs. trans*) also plays a decisive role, with measurable consequences for precursor performance. Although the precise weighting of geometry relative to molecular weight and branching remains difficult to quantify, our results establish a clear connection between structural arrangement and the phase and morphology of deposited films. Future studies employing *cis*/*trans* or *fac*/*mer* variants of identical ligand sets will allow these factors to be disentangled more rigorously and other substrates could be utilised for nucleation studies.

Proof of- -principle depositions using precursors (**A**) and (**B**) yielded copper sulfide digenite with a covellite surface component, confirming that this ligand class can function as viable single source precursors under solvent- free thermal conditions. Vapour pressure analysis using Knudsen and Clausius–Clapeyron approaches provides a foundation for scaling these systems to -reactor based- CVD or ALD processes. Importantly, precursor (**A**) produced larger crystallites and more uniform films, suggesting suitability for optoelectronic and photovoltaic applications where reduced grain boundary density enhances charge transport. In contrast, precursor (**B**) generated smaller crystallites and clustered growth, which may be advantageous for catalytic or sensing applications where high grain boundary density increases surface reactivity.

Overall, *N*,*N*-disubstituted-*N*′-acylthiourea complexes as precursors emerge as a versatile and tuneable platform for copper sulfide deposition. Their solid state- stability, sufficient vapour pressure, and structural flexibility distinguish them from established SSP classes such as thiolates or dithiocarbamates. With targeted ligand modifications, this family offers a promising route to tailor volatility and film morphology, positioning them as competitive candidates for next generation thin-film and nanostructured material applications.

Experimental

General synthesis for ligands and metal complexes

The ligands, and the copper(II) complexes, were prepared by adapting from previously reported synthesis.[55–57]

Materials synthesis and analysis

SEM imaging was carried out using a Zeiss Supra 40 high resolution SEM at typical acceleration voltages of 15–20 kV. The instrument was used to analyse the morphology and thickness of the deposited materials. Dimensional analysis for feature size distributions from SEM images were measured using ImageJ software. Energy dispersive X-ray spectroscopy (EDX) analysis was also performed on the same SEM instrument using accelerating voltage of 15 kV.

X-ray diffraction (XRD) was carried out using a Rigaku Miniflex 600, equipped with a Cu anode X-ray tube with fine focus and a D/teX Ultra 2 detector.

Growth studies (proof of concept)

Growth experiments was carried out in an Elite Thermal Systems Ltd Tube Furnace with controlled heating at 230 °C for precursor (**A**) and 190 °C for precursor (**B**). Pre-cut silicon wafers (20 mm × 15 mm) & (20 mm × 10 mm) were selected as substrates and pre-treated with acetone, isopropyl alcohol and dried over argon. The precursor(s) were placed into a crucible approxiamtely 0.5 grams with a silicon wafer resting on the top (5 mm above the loaded precursor); note the wafer did not cover the entire crucible. The tube furnace was left at the set temperature for 3 hours. Samples were removed once they had cooled to room temperature. Note not all the precursor sample appeared to have been volatilised, residual precursor remained inside the alumina crucibles.

Thermal analysis

Differential scanning calorimetry (DSC) data were collected using a TA Instruments Q1000. Samples (2–6 mg) were crimped in non-hermetic aluminium pans and scanned from 30 to 250 °C at a heating rate of 10 °C min^{-1} under a continuously purged dry nitrogen atmosphere.

Thermogravimetric Analysis was performed on a TA Q500 series. Samples were loaded onto a platinum crucible of 10 mm. Samples were heated from 30–600 °C at a heating rate of 10 °C min^{-1} under a continuously purged dry nitrogen atmosphere.

Conflicts of interest

There are no conflicts to declare.

Data availability

The data supporting this article have been included as part of the supplementary information (SI). Supplementary information: biological toxicity screening, table of copper sulfur single source precursors, stacked DSC analysis of the nine copper(II) complexes, isothermal data of the selected precursors (A & B), proof of principle materials deposition, further experimental information. See DOI: https://doi.org/10.1039/d4dt03482a.

Acknowledgements

This work was supported by Science Foundation Ireland, SFI Grant Principal Investigator Project Number 15/IA/3015 'Design, Deposition and Exploitation of Novel Micro and Nano-scale Materials and Devices for Advanced Manufacturing- DEPO-Man'. The authors wish to acknowledge the late Simon Rushworth for his input, help and guidance on the vapour pressure calculations. "The antimicrobial toxicity screening performed by CO-ADD (The Community for Antimicrobial Drug Discovery) was funded by the Wellcome Trust (UK) and The University of Queensland (Australia)". Helping Chemists Discover New Antibiotics M. A. Blaskovich, J. Zuegg, A. G. Elliott and M. A. Cooper, *ACS Infect. Dis.*, 2015, 1(7), 285–287. https://doi.org/10.1021/acsinfecdis.5b00044; PMID: 27622818.

References

1 W. Niu, X. Li, S. K. Karuturi, D. W. Fam, H. Fan, S. Shrestha, L. H. Wong and A. I. Tok, *Nanotechnology*, 2015, **26**, 64001.
2 N. P. Dasgupta, X. Meng, J. W. Elam and A. B. F. Martinson, *Acc. Chem. Res.*, 2015, **48**, 341–348.
3 M. Mousavi-Kamazani, Z. Zarghami and M. Salavati-Niasari, *J. Phys. Chem. C*, 2016, **120**, 2096–2108.
4 J. A. Hollingsworth, K. K. Banger, M. H.-C. Jin, J. D. Harris, J. E. Cowen, E. W. Bohannan, J. A. Switzer, W. E. Buhro and A. F. Hepp, *Thin Solid Films*, 2003, **431–432**, 63–67.
5 K. K. Banger, J. A. Hollingsworth, J. D. Harris, J. Cowen, O. William, E. Buhro and A. F. Hepp, *Single Source Precursors for Thin Film Solar Cells*, 2002.
6 K. K. Banger, J. Cowen, J. Harris, R. Mcclamon, D. G. Hehemann, S. A. Duraj, D. Scheiman and A. F. Hepp, *A review of single source precursors for the deposition of ternary chalcopyrite materials*, 2003.
7 M. A. Agoro and E. L. Meyer, *Inorganics*, 2023, **11**, 266–284.
8 M. A. Agoro, E. L. Meyer, J. Z. Mbese and K. Manu, *Catalysts*, 2020, **10**, 300.
9 G. Karmakar, A. Tyagi, K. K. Halankar, S. Nigam, B. P. Mandal, A. P. Wadawale, G. Kedarnath and A. K. Debnath, *Dalton Trans.*, 2023, **52**, 1461–1475.
10 Y. Shi, B. Yang, X. Guo, X. Wu and H. Pang, *Mater. Today Chem.*, 2022, **23**, 100675.
11 U. Shamraiz, R. A. Hussain and A. Badshah, *J. Solid State Chem.*, 2016, **238**, 25–40.
12 O. C. Olatunde and D. C. Onwudiwe, *Front. Mater.*, 2021, **8**, 687562.
13 S. P. Yadav, G. Karmakar, A. Y. Shah, B. G. Vats, A. Pathak, A. Tyagi, R. S. Chauhan and V. Singh, *RSC Adv.*, 2024, **14**, 22656–22664.
14 N. ul Ain, J. A. Nasir, Z. Khan, I. S. Butler and Z. Rehman, *RSC Adv.*, 2022, **12**, 7550–7567.
15 A. T. Khalil, M. D. Khan, S. Razzaque, S. Afridi, I. Ullah, J. Iqbal, S. Tasneem, A. Shah, Z. K. Shinwari, N. Revaprasadu and M. Ayaz, *Appl. Nanosci.*, 2021, **11**, 2489–2502.
16 J. Chen, Z. Xu and Y. Chen, in *Electronic Structure and Surfaces of Sulfide Minerals*, ed. J. Chen, Z. Xu and Y. Chen, Elsevier, 2020, pp. 13–81.
17 P. Leidinger, R. Popescu, D. Gerthsen, H. Lünsdorf and C. Feldmann, *Nanoscale*, 2011, **3**, 2544–2551.
18 K. Ramasamy, M. A. Malik, M. Helliwell, J. Raftery and P. O'Brien, *Chem. Mater.*, 2011, **23**, 1471–1481.
19 M. Isik, M. Terlemezoglu, N. Gasanly and M. Parlak, *Phys. E*, 2022, **144**, 115407.
20 J. N. Solanki, R. Sengupta and Z. V. P. Murthy, *Solid State Sci.*, 2010, **12**, 1560–1566.
21 M. Kemmler, M. Lazell, P. O'Brien, D. J. Otway, J.-H. Park and J. R. Walsh, *J. Mater. Sci.: Mater. Electron.*, 2002, **13**, 531–535.
22 N. L. Pickett and P. O'Brien, *Chem. Rec.*, 2001, **1**, 467–479.
23 M. Lazell, P. O'Brien, D. J. Otway and J.-H. Park, *J. Chem. Soc., Dalton Trans.*, 2000, 4479–4486.
24 G. Barone, T. G. Hibbert, M. F. Mahon, K. C. Molloy, L. S. Price, I. P. Parkin, A. M. E. Hardy and M. N. Field, *J. Mater. Chem.*, 2001, **11**, 464–468.
25 K. Ramasamy, V. L. Kuznetsov, K. Gopal, M. A. Malik, J. Raftery, P. P. Edwards and P. O'Brien, *Chem. Mater.*, 2013, **25**, 266–276.
26 M. D. Regulacio, N. Tomson and S. L. Stoll, *Chem. Mater.*, 2005, **17**, 3114–3121.
27 M. A. Buckingham, A. L. Catherall, M. S. Hill, A. L. Johnson and J. D. Parish, *Cryst. Growth Des.*, 2017, **17**, 907–912.
28 M. A. Malik, M. Afzaal and P. O'Brien, *Chem. Rev.*, 2010, **110**, 4417–4446.
29 K. Ramasamy, M. A. Malik, J. Raftery, F. Tuna and P. O'Brien, *Chem. Mater.*, 2010, **22**, 4919–4930.
30 K. Ramasamy, M. A. Malik, P. O'Brien, J. Raftery and M. Helliwell, *Chem. Mater.*, 2010, **22**, 6328–6340.
31 H. S. I. Sullivan, J. D. Parish, P. Thongchai, G. Kociok-Kohn, M. S. Hill and A. L. Johnson, *Inorg. Chem.*, 2019, **58**, 2784–2797.
32 Z. Ali, N. E. Richey, D. C. Bock, K. A. Abboud, J. Akhtar, M. Sher and L. McElwee-White, *Dalton Trans.*, 2018, **47**, 2719–2726.
33 C. Gervas, S. Mlowe, M. P. Akerman and N. Revaprasadu, *New J. Chem.*, 2018, **42**, 6203–6209.

34 S. Schneider, Y. Yang and T. J. Marks, *Chem. Mater.*, 2005, **17**, 4286–4288.
35 S. Schneider, J. A. S. Roberts, M. R. Salata and T. J. Marks, *Angew. Chem., Int. Ed.*, 2006, **45**, 1733–1736.
36 G. Karmakar, A. Y. Shah, M. Kumar, V. Singh, G. K. Kole and A. Tyagi, *J. Mol. Struct.*, 2024, **1295**, 136707.
37 A. Singh, M. Trivedi, P. Singh, G. Kociok-Köhn, U. P. Azad, A. K. Singh and A. Kumar, *New J. Chem.*, 2018, **42**, 18759–18764.
38 M. D. Khan, M. A. Malik, J. Akhtar, S. Mlowe and N. Revaprasadu, *Thin Solid Films*, 2017, **638**, 338–344.
39 S. N. Malik, A. Q. Malik, R. F. Mehmood, G. Murtaza, Y. G. Alghamdi and M. A. Malik, *New J. Chem.*, 2015, **39**, 4047–4054.
40 S. N. Malik, A. Q. Malik, R. F. Mehmood, G. Murtaza, Y. G. Alghamdi and M. A. Malik, *New J. Chem.*, 2015, **39**, 4047–4054.
41 H. Trabelsi, I. Gràcia, K. Alouani and S. Vallejos, *Ceram. Int.*, 2025, **51**, 1949–1957.
42 M. D. Khan, M. Akhtar, M. A. Malik, N. Revaprasadu and P. O'Brien, *ChemistrySelect*, 2018, **3**, 2943–2950.
43 R. Nomura, K. Kanaya and H. Matsuda, *Ind. Eng. Chem. Res.*, 1989, **28**, 877–880.
44 R. Nomura, K. Miyawaki, T. Toyosaki and H. Matsuda, *Chem. Vap. Deposition*, 1996, **2**, 174–179.
45 S. Saeed and R. Hussain, *Eur. Chem. Bull.*, 2013, **2**, 465–467.
46 S. Saeed, N. Rashid, R. Hussain, M. A. Malik, P. O'Brien and W.-T. Wong, *New J. Chem.*, 2013, **37**, 3214–3221.
47 K. I. Y. Ketchemen, M. D. Khan, S. Mlowe, L. D. Nyamen, P. T. Ndifon, P. O'Brien and N. Revaprasadu, *J. Inorg. Organomet. Polym. Mater.*, 2019, **29**, 917–927.
48 T. Hatanpää, M. Ritala and M. Leskelä, *Coord. Chem. Rev.*, 2013, **257**, 3297–3322.
49 M. A. Malik and P. O'Brien, in *Chemical Vapour Deposition*, 2008, pp. 207–271.
50 S. E. Koponen, P. G. Gordon and S. T. Barry, *Polyhedron*, 2016, **108**, 59–66.
51 H. O. Pierson, *Handbook of chemical vapor deposition: principles, technology and applications*, William Andrew, 1999.
52 G. Fang, L. Xu, Y. Cao and A. Li, *Coord. Chem. Rev.*, 2016, **322**, 94–103.
53 A. Devi, *Coord. Chem. Rev.*, 2013, **257**, 3332–3384.
54 S.-Y. Wu, X.-Y. Zhao, H.-P. Li, Y. Yang and H. W. Roesky, *Z. Anorg. Allg. Chem.*, 2015, **641**, 883–889.
55 C. K. Ozer, H. Arslan, D. Vanderveer and G. Binzet, *J. Coord. Chem.*, 2009, **62**, 266–276.
56 S. Saeed, N. Rashid, J. P. Jasinski, R. J. Butcher and H. Rizwan, *Acta Crystallogr., Sect. E: Struct. Rep. Online*, 2010, **66**, o2589.
57 W. Daly, M. E. Pemble, D. Tiana and D. J. Otway, *J. Mol. Struct.*, 2026, **1349**, 143678.